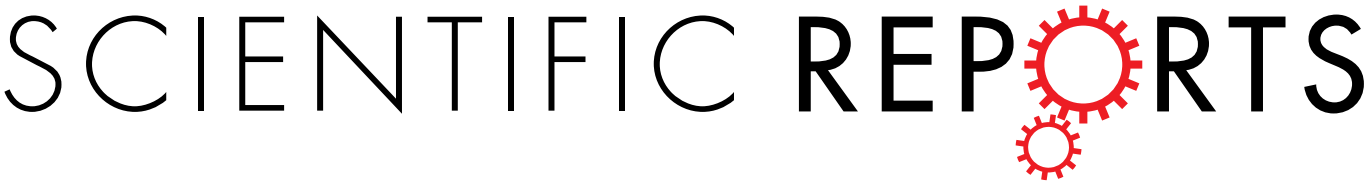

OPEN

Received: 22 November 2016
Accepted: 25 April 2017
Published online: 09 June 2017

# Synthesis, Chemical Characterization and Multiscale Biological Evaluation of a Dimeric-cRGD Peptide for Targeted Imaging of $\alpha_V\beta_3$ Integrin Activity

Jamila Hedhli[1,2], Andrzej Czerwinski[3], Matthew Schuelke[1,2], Agata Płoska[1,4], Paweł Sowinski[5], Lukas La Hood[1,2], Spencer B. Mamer[2], John A. Cole[6], Paulina Czaplewska[7], Maciej Banach[8], Iwona T. Dobrucki[1], Leszek Kalinowski[4], Princess Imoukhuede[2] & Lawrence W. Dobrucki[1,2]

**Cyclic peptides containing the Arg-Gly-Asp (RGD) sequence have been shown to specifically bind the angiogenesis biomarker $\alpha_V\beta_3$ integrin. We report the synthesis, chemical characterization, and biological evaluation of two novel dimeric cyclic RGD-based molecular probes for the targeted imaging of $\alpha_V\beta_3$ activity (a radiolabeled version, $^{64}$Cu-NOTA-PEG$_4$-cRGD$_2$, for PET imaging, and a fluorescent version, FITC-PEG$_4$-cRGD$_2$, for *in vitro* work). We investigated the performance of this probe at the receptor, cell, organ, and whole-body levels, including its use to detect diabetes associated impairment of ischemia-induced myocardial angiogenesis. Both versions of the probe were found to be stable, demonstrated fast receptor association constants, and showed high specificity for $\alpha_V\beta_3$ in HUVECs ($K_d$ ~ 35 nM). Dynamic PET-CT imaging indicated rapid blood clearance via kidney filtration, and accumulation within $\alpha_V\beta_3$-positive infarcted myocardium. $^{64}$Cu-NOTA-PEG$_4$-cRGD$_2$ demonstrated a favorable biodistribution, slow washout, and excellent performance with respect to the quality of the PET-CT images obtained. Importantly, the ratio of probe uptake in infarcted heart tissue compared to normal tissue was significantly higher in non-diabetic rats than in diabetic ones. Overall, our probes are promising agents for non-invasive quantitative imaging of $\alpha_V\beta_3$ expression, both *in vitro* and *in vivo*.**

The development of capillaries from preexisting vessels to form new vasculature, termed as angiogenesis, is tightly controlled by a delicate balance of pro- and anti-angiogenic factors. The main stimulators of blood vessel formation are vascular endothelial growth factor (VEGF) and basic fibroblast growth factor (bFGF), while endogenous inhibitors include thrombospondin, and angiostatin[1]. The process of creating new blood vessels is necessary for physiological function, but is also a hallmark of many pathological disorders such as inflammation, ischemic heart disease, and cancer.

Over the last two decades, significant research efforts have been directed at developing novel targeted imaging techniques for the non-invasive assessment of angiogenesis as a tool for early diagnosis, prognostication, and monitoring of novel individualized therapeutic interventions focused on the modulation of the angiogenic process[2]. These efforts resulted in the discovery of numerous potential imaging targets including integrins, which play an important role in the regulation of angiogenesis[3]. Found in species ranging from sponges to mammals, integrins are heterodimer transmembrane glycoproteins consisting of $\alpha$ (150–180 kD) and $\beta$ (90 kD) subunits.

[1]Beckman Institute for Advanced Science and Technology, Urbana, IL, USA. [2]Department of Bioengineering, University of Illinois at Urbana-Champaign, Urbana, IL, USA. [3]Peptides International Inc., Louisville, KY, USA. [4]Department of Laboratory Diagnostics, Medical University of Gdansk, Gdansk, Poland. [5]NMR Laboratory, Faculty of Chemistry, Gdansk University of Technology, Gdansk, Poland. [6]Department of Physics, University of Illinois at Urbana-Champaign, Urbana, IL, USA. [7]Intercollegiate Faculty of Biotechnology of the University of Gdansk and Medical University of Gdansk, Gdansk, Poland. [8]Department of Hypertension, Medical University of Lodz, Lodz, Poland. Jamila Hedhli and Andrzej Czerwinski contributed equally to this work. Correspondence and requests for materials should be addressed to L.W.D. (email: dobrucki@illinois.edu)

The cell surface receptor is composed of three parts: a large ectodomain, a single transmembrane domain, and a short cytoplasmic tail. Integrins, when activated by an intracellular ligand (*e.g.* talin or kindlin), become capable of binding specific extracellular molecules in a unique combination of "inside-out" and "outside-in" signaling. In response, the integrins elicit a cascade of biochemical events that modulate gene expression, and regulate cytoskeleton organization[4–6].

Significant effort has been expended exploring the clinical utility of imaging $\alpha_V\beta_3$[7,8] expression associated with tumor angiogenesis and metastatic dissemination[9,10]. For example, radiolabeled integrin peptide ligands with a pentapeptide motif Arg-Gly-Asp-Phe-Lys (RGDfK) have been used as tools in research aimed at developing radiotracers for clinical applications[11,12]. Numerous linear and cyclic RGD peptides based (to a greater or lesser extent) on the RGDfK motif, in combination with a variety of pharmacokinetic modifiers, prosthetic groups or bifunctional chelators and radionuclides have been reported and used as diagnostic probes in animal studies and clinical investigations in the areas of oncology[13–23] and cardiology[24–27].

Multivalent interactions have been shown to play a key role in many biological processes[28]. This phenomenon was behind the rationale for the design of multimeric cRGD ligands. A series of such peptides labeled with $^{18}$F, $^{64}$Cu and $^{68}$Ga for PET or $^{99m}$Tc for SPECT imaging have been reported[29–33]. They demonstrated higher receptor binding affinity *in vitro* and better tumor retention *in vivo* when compared to their corresponding monomeric counterparts. PEG and other types of linkers have been employed as pharmacokinetic modifiers, resulting in significantly increased tumor uptake and enhanced clearance from noncancerous organs[34–38]. Comparisons of different RGD-based tracers have demonstrated that increasing the peptide multiplicity can greatly improve affinity, but above a certain threshold, highly multimeric compounds exhibit non-specific organ uptake that can limit their applicability as imaging agents. This led to the conclusion that the dimeric subclass of the RGD peptides is an optimal choice for the development of imaging agents for clinical applications[15,23,39]. The SPECT tracer $^{99m}$Tc-3PRGD$_2$[34,40–43] as well as several RGD-based PET radiotracers[44–48], have already entered clinical investigation stage[12].

In the design of our new $\alpha_V\beta_3$ targeted probe we integrated several structural elements known for their positive impact on pharmacokinetic properties including PEG moieties and 1,2,3-triazole residues[49]. Here we report the synthesis and chemical characterization of $\alpha_V\beta_3$ integrin targeted $^{64}$Cu-labeled dimeric-cRGD probe (designed for *in vivo* PET imaging) and its FITC-labeled fluorescent analogue (designed for *in vitro* imaging with single-cell resolution). Using established *in vitro* and *in vivo* models we evaluated its efficacy as an imaging agent at the receptor, single cell, organ, and whole-body levels with the emphasis on quantitative assessment of $\alpha_V\beta_3$ integrin expression in diabetic and non-diabetic rats following myocardial infarction (MI).

## Results

**Synthesis and Chemical Characterization.** The synthesis (Supplementary Figure S1) began with coupling of $N_3$-$PEG_2$-OH to a selectively protected cyclopentapeptide, yielding azidopegylated protected peptide (**1**). An important aspect of our design was related to the dimerization method. Dimeric peptides have usually been prepared by an acylation reaction using cRGD monomers and N-protected glutamic acid active esters, e.g. Boc-Glu(OSu)$_2$ as the substrates[30,31,50]. In our case, the dimerization was achieved by employing Boc-glutamic acid bis-propargyl amide as an alkyne substrate to bridge two RGD pegylated cyclopentapeptides via the copper (I)-catalyzed 1,3-dipolar Huisgen cycloaddition, yielding the protected product (**2**). This is only the second synthesis of the cRGD dimer, after galacto-RGD$_2$, based on the aforementioned click reaction protocol[38]. Total deprotection of (**2**), followed by the PEGylation reaction using Boc-$PEG_4$-OSu, and Boc-group removal yielded compound (**5**). After RP-HPLC preparative purification, product (**5**) was used as the substrate for the synthesis of both tracers, $^{64}$Cu-NOTA-$PEG_4$-cRGD$_2$ (**7**) and fluorescent analogue FITC-$PEG_4$-cRGD$_2$ (**8**). Briefly, product (**7**) was prepared in the reaction of (**5**) with p-SCN-Bn-NOTA, followed by the radiolabeling of NOTA-chelated compound (**6**). Reaction of (**5**) with fluorescein-5- isothiocyanate yielded the fluorescent product (**8**). Based on the $^1$H, $^{13}$C, DQF-COSY, TOCSY, NOESY NMR and H/C correlation spectra (gHSQC and gHMBC, Supplementary Figures S2–S8), a full structural analysis of NOTA-$PEG_4$-cRGD$_2$ (**6**) was performed, including assignment of all proton and carbon resonances (Supplementary Tables S2 and S3). To confirm the successful synthesis and measure masses of NOTA-$PEG_4$-cRGD$_2$ (**6**) and FITC-$PEG_4$-cRGD$_2$ (**8**) see (Fig. 1), high-resolution MS spectra for pure products were registered in direct infusion mode. For product (**6**) the three- and four-fold charged molecular ions were identified on ESI spectrum (Supplementary Figure S8).

**Dimeric cRGD Probe Binds Preferentially to the $\alpha_V\beta_3$ Integrin Receptor.** *Receptor binding kinetics.* We investigated the receptor binding kinetics of both the FITC- and $^{64}$Cu-labeled tracers using surface plasmon resonance (SPR). As described in Methods and Supporting Information sections, initial pre-concentration studies were focused on adjusting the pH to optimize protein immobilization. We then evaluated the association and dissociation rates of our probes to the immobilized $\alpha_V\beta_3$ receptors and compared these values with those of a commercially available monomeric probe, cRGDyK.

The SPR sensograms associated with each probe demonstrated significant accumulation upon initial injection (Fig. 2). Their association phases were characterized by a sharp signal increase at the start of the injection, followed by a slow decrease following the injection. We observed that unlabeled dimeric probe bound $\alpha_V\beta_3$ with an affinity ($K_d$) approximately 50 times greater than the monomeric cRGD (Table 1), which was paralleled by a larger magnitude response $R_{max} = 10$ R.U. (Fig. 2B) compared to ~5 R.U. (Fig. 2A). Both labeled versions of our probe showed only marginally reduced binding affinity for $\alpha_V\beta_3$ relative to the unlabeled version, but they both outperformed the monomeric cRGD-based probe.

*Binding affinity in HUVECs.* We next studied the cellular binding properties of both (**7**) and (**8**). For our studies we used human umbilical vein endothelial cells (HUVECs), which are known to constitutively express

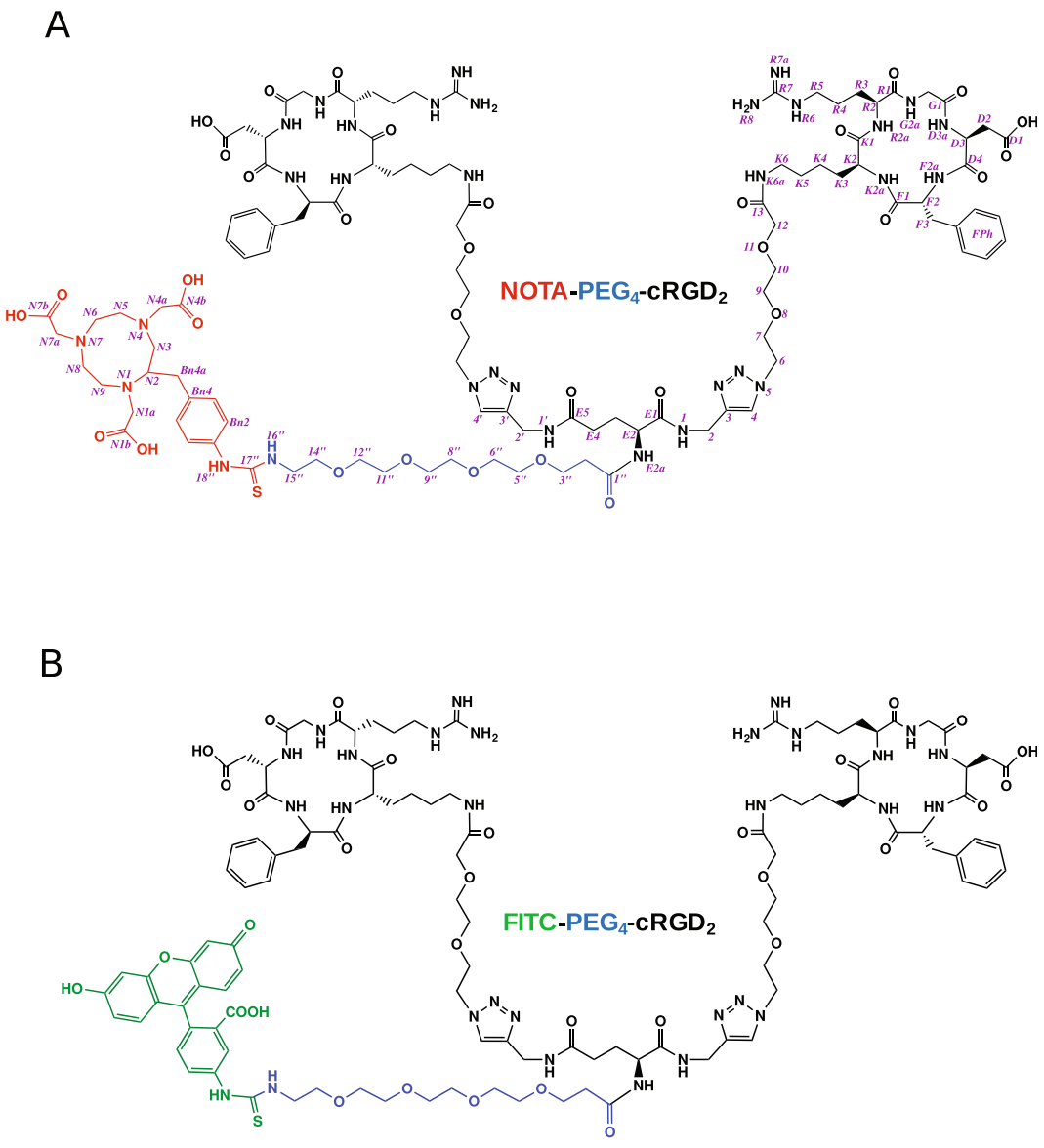


**Figure 1.** Chemical structures of (**A**) NOTA-$PEG_4$-$cRGD_2$ and (**B**) FITC-$PEG_4$-$cRGD_2$.

$\alpha_V\beta_3$ integrin. HUVECs were first treated with (**8**) and co-incubated with the anti- $\alpha_V\beta_3$ antibody. Subsequent two-channel confocal fluorescent microscopic images (Fig. 3A–C) demonstrated a significant degree of overlap between the fluorescein and phycoerythrin signals (Pearson's coefficient $\rho = 0.87$), which indicates a strong co-localization of (**8**) with $\alpha_V\beta_3$ integrin receptor. The specificity of (**8**) was further assessed on a single cell level using flow cytometry. Figure 3D shows a quadrant plot of HUVECs treated with (**8**) and co-incubated with the anti- $\alpha_V\beta_3$ antibody, which showed that (**8**) successfully bound over 99% of HUVECs expressing $\alpha_V\beta_3$ integrin. To quantitatively evaluate binding parameters, cultured HUVECs were incubated with various concentrations of (**7**) and (**8**) followed by cellular binding assay with gamma well counting and flow cytometry. The observed radioactivity and fluorescence intensity was found to increase with probe concentration and fit well to a Hill-type function (Fig. 4A and B). This allowed us to estimate the dissociation constant ($K_d$) at 38.27 nM and 33.85 nM for the (**8**) and (**7**), respectively. We also compared our (**8**) to a commercially available probe FITC-Galacto-$cRGD_2$ and found similar binding kinetics (Fig. 4C). Both (**7**) and (**8**) also showed strong correlation ($R^2 = 0.95$) over the range of concentrations used in the cellular binding experiments (Fig. 4D).

*Binding affinity in the presence of metal ions.* We incubated HUVECs with either 20 $\mu$M of $Mn^{2+}$ or EDTA and measured the $B_{max}$ and $K_d$ with flow cytometry and gamma well counting. The maximum fraction of bound receptors was found to decrease in the presence of EDTA (Fig. 4) for both probes. Interestingly, the $^{64}$Cu-labeled probe showed a significantly more pronounced decrease in $B_{max}$, which we attribute to the scavenging of $^{64}$Cu by EDTA. The dissociation constants for both the $^{64}$Cu- and FITC-labeled probes in the presence of EDTA were measured to be approximately 55 nM, indicating a similar effect on the binding kinetics. In the presence of $Mn^{2+}$

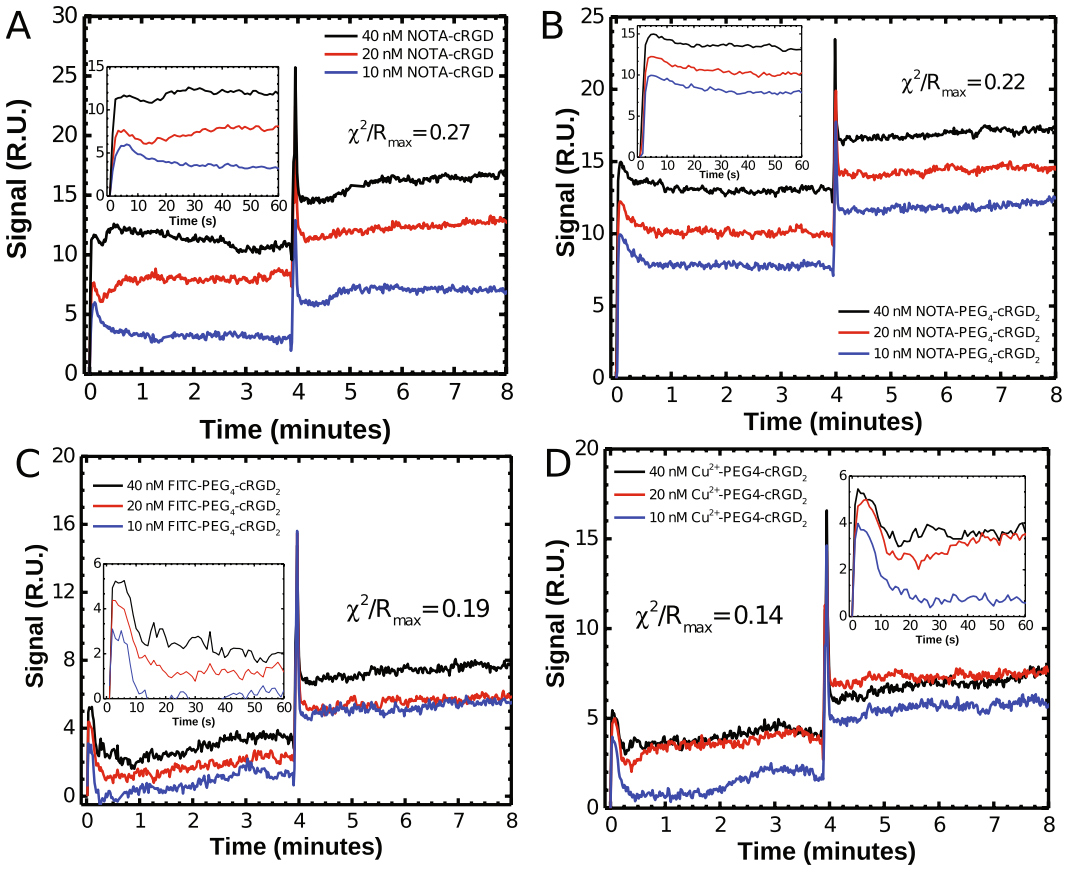


**Figure 2.** SPR sensograms depicting binding between cRGD ligands and $\alpha_V\beta_3$ integrin receptor. BIAcore 3000 kinetics studies of interactions between immobilized integrin $\alpha_V\beta_3$ receptor and (**A**) monomeric cyclic RGD probe (NOTA-cRGD), (**B**) dimeric cyclic RGD (NOTA-$PEG_4$-$cRGD_2$) probe, (**C**) $cRGD_2$ conjugated with FITC (FITC-$PEG_4$-$cRGD_2$), and (**D**) NOTA-$PEG_4$-$cRGD_2$ labeled with non-radioactive $Cu^{2+}$. Kinetic studies were performed at a 30 $\mu$ L/min flow rate, with a 4 min association followed by a 10 min dissociation period.

| Probe | $K_{on}$ ($M^{-1}$ $s^{-1}$) | $K_{off}$ ($s^{-1}$) | $K_D$ (pM) | $\chi^2/Rmax$ |
|---|---|---|---|---|
| NOTA-cRGD | $2.7 \times 10^5$ | $2.6 \times 10^{-6}$ | 9.6 | 0.26 |
| NOTA-$PEG_4$-$cRGD_2$ | $1.1 \times 10^7$ | $2.1 \times 10^{-6}$ | $1.9 \times 10^{-1}$ | 0.22 |
| FITC-$PEG_4$-$cRGD_2$ | $7.6 \times 10^5$ | $6.6 \times 10^{-6}$ | 8.6 | 0.19 |
| $^{64}$Cu-NOTA-$PEG_4$-$cRGD_2$ | $7.1 \times 10^5$ | $1.1 \times 10^{-6}$ | 1.5 | 0.14 |

**Table 1.** Summary of binding affinity and kinetic rates measured between cRGD-based monomeric and dimeric probes and immobilized integrin $\alpha_V\beta_3$ receptor using a surface plasmon resonance-based approach. Kinetic constants were obtained by performing global kinetic analysis using the BIAevaluation software across several kinetic binding sensograms for each ligand-receptor pair.

the probes' binding was found to increase by 78% when compared to HUVECs incubated without $Mn^{2+}$ (Fig. 4E and F). Likewise, the dissociation constant in the presence of $Mn^{2+}$ was considerably lower reaching 13.8 nM.

*Competitive binding.* Finally, we studied competitive $\alpha_V\beta_3$ integrin binding properties for our dimeric-cRGD probes. HUVECs were pre-treated with an excess of unlabeled NOTA-$PEG_4$-$cRGD_2$ (50 $\mu$M) followed by incubation with various concentrations of (**7**) or (**8**). This resulted in a noticeable decrease in $B_{max}$ and an increase in the $K_d$ (188 nM) compared to untreated cells (Fig. 4A,B). To determine $IC_{50}$ values, HUVEC were treated with a fixed concentration of the probe (50 nM) and incubated with a range of unlabeled NOTA-$PEG_4$-$cRGD_2$ concentrations. The results of these experiments were fit to a model of homologous inhibition and yielded an approximate $IC_{50}$ of 5.1 nM (Fig. 4G)[51].

**Pharmacokinetics, Biodistribution, and PET Imaging.** Dynamic *in vivo* PET-CT imaging of $\alpha_V\beta_3$ integrin activity (Fig. 5A) demonstrated favorable initial biodistribution and clearance kinetics for (**7**). Clearance kinetics from critical organs during the first 60 min after injection was quantified by placing volumes of interest (VOIs) on the dynamic co-registered PET-CT image sets. The radioactivity within these VOIs was expressed as

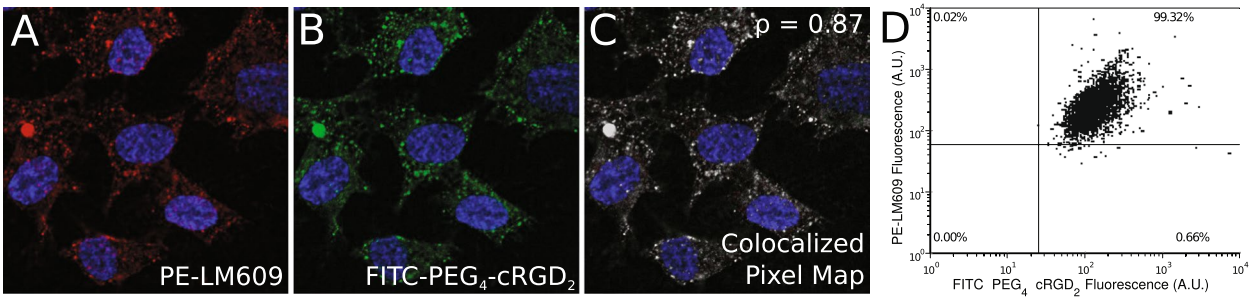


**Figure 3.** Colocalization between phycoerythrin-labeled anti- $\alpha_V\beta_3$ integrin primary antibody (PE-LM609) and FITC-labeled $PEG_4$-$cRGD_2$ probe. Human umbilical vein endothelial cells (HUVEC) were grown to confluency and incubated with both PE-LM609 and FITC-$PEG_4$-$cRGD_2$. Fluorescence microscopy images were acquired in DAPI/PE (**A**) and DAPI/FITC (**B**) channels and were superimposed to create colocalized pixel map (**C**) to calculate Pearson's coefficient. Flow cytometric analysis of HUVEC co-incubated with PE-LM609 and FITC-$PEG_4$-$cRGD_2$ demonstrated a very high degree of colocalization between integrin $\alpha_V\beta_3$ and FITC-$PEG_4$-$cRGD_2$ probe (**D**).

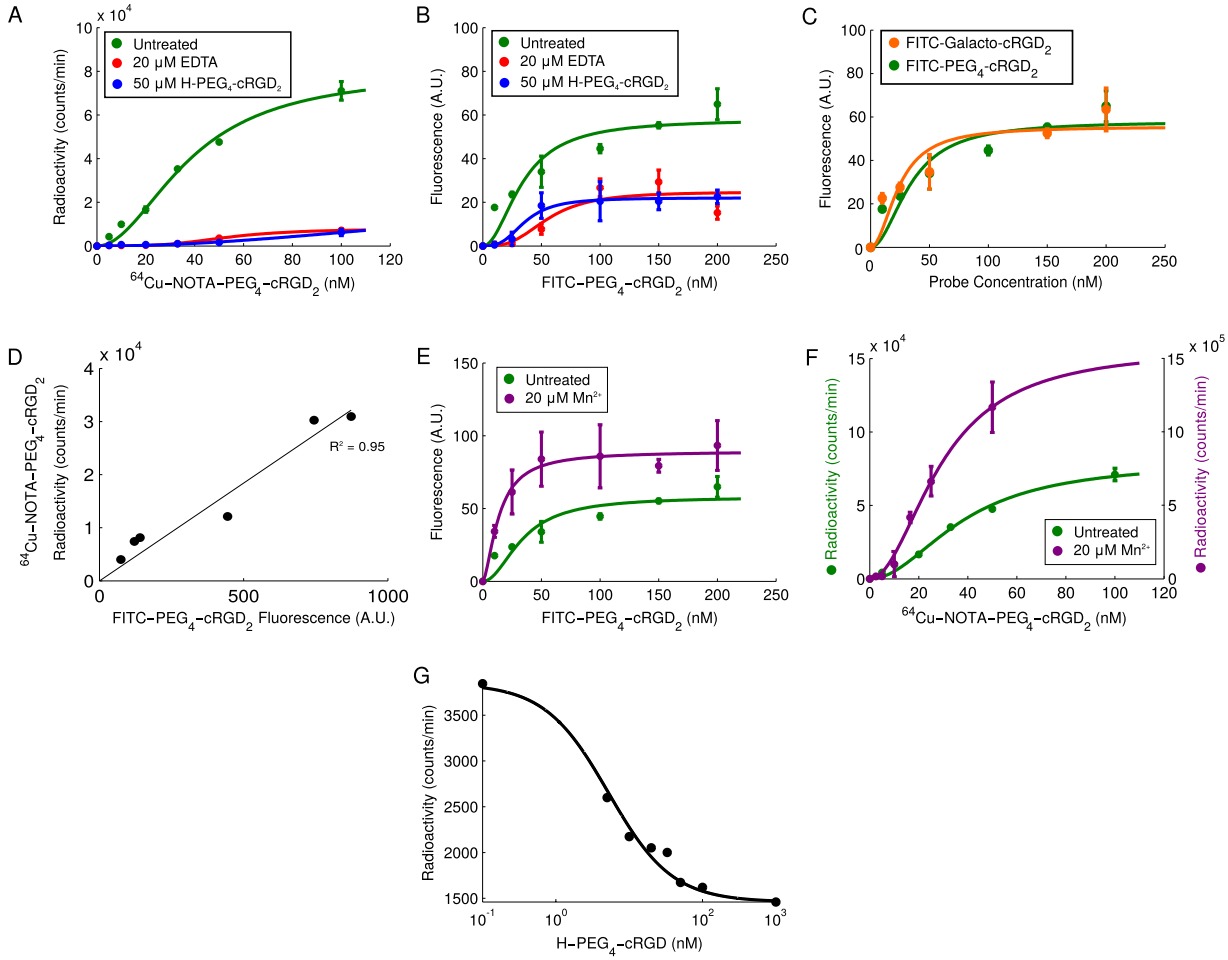


**Figure 4.** Binding kinetics of FITC and $^{64}Cu$ labeled $cRGD_2$ probes. (**A**) Radioactivity of confluent HUVEC cells incubated with varying concentrations of $^{64}Cu$-NOTA-$PEG_4$-$cRGD_2$ (green) and with either 20 $\mu$M EDTA (red) or 50 $\mu$M of H-$PEG_4$-$cRGD_2$ (blue). (**B**) Fluorescence of the FITC-$PEG_4$-$cRGD_2$ (green) with either 20 $\mu$M EDTA (red) or 50 $\mu$M of H-$PEG_4$-$cRGD_2$ (blue). (**C**) Comparison of the fluorescence of the FITC-$PEG_4$-$cRGD_2$ (green) with FITC-Galacto-$cRGD_2$ (orange). (**D**) Correlation between FITC and $Cu^{64}$ labeled $cRGD_2$ probes bound to HUVECs. (**E**) The fluorescence of HUVEC cells incubated with varying concentrations of FITC-$PEG_4$-$cRGD_2$ (green) and co-incubated with 20 $\mu$M of $Mn^{2+}$ (purple). (**F**) Radioactivity of confluent HUVEC cells incubated with varying concentrations of $^{64}Cu$-NOTA-$PEG_4$-$cRGD_2$ (green) and co-incubated with 20 $\mu$M of $Mn^{2+}$ (purple). (**G**) Competition binding between $^{64}Cu$-NOTA-$PEG_4$-$cRGD_2$ (50 nM) and increasing concentrations of unlabeled H-$PEG_4$-$cRGD_2$ in HUVEC cells.

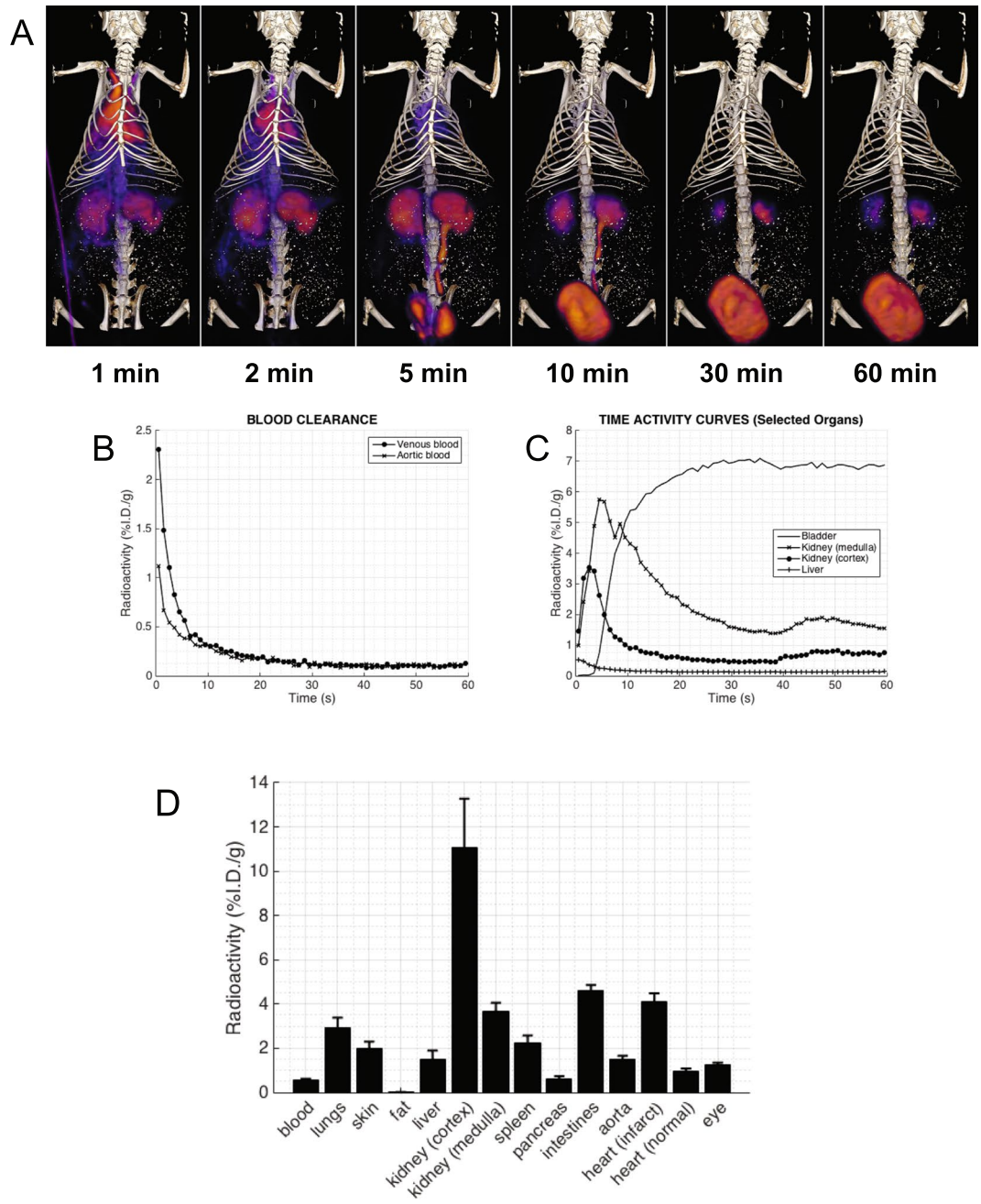


**Figure 5.** Dynamic PET-CT images (**A**) were used to plot the blood clearance (**B**) and time activity curves (TAC) of $^{64}$Cu-NOTA-PEG$_4$-cRGD$_2$ in selected organs (**C**). (**D**) Biodistribution of $^{64}$Cu-NOTA-PEG$_4$-cRGD$_2$ in selected organs at 90 min post-injection in Lewis rats subjected to myocardial infarction induced by surgical ligation of LAD. Results are expressed in percentage of injected dose per gram tissue (%I.D./g). These results suggest a rapid blood clearance through renal filtration and very low non-specific uptake in other critical organs.

percent injected dose per gram tissue (%I.D./g). The representative blood and tissue activity curves are shown in (Fig. 5B and C). After intravascular injection, (**7**) cleared rapidly from the blood, accumulated primarily in the kidneys, and was excreted in the urine, which was retained in the bladder as early as 15 min after injection.

Figure 5D shows the biodistribution data of (**7**) at 90 min after intravascular injection into control rats and animals subjected to the LAD ligation. As expected, the highest uptake was observed in the kidneys due to renal filtration being the dominate excretion route ($11.08 \pm 2.20$ and $3.66 \pm 0.40$ %I.D./g for cortex and medulla, respectively). Relatively high uptake was also observed in the intestines ($4.62 \pm 0.24$), lungs ($2.95 \pm 0.43$), and the spleen ($2.25 \pm 0.33$).

To assess *in vivo* stability of (**7**) we performed metabolism studies at the end of the dynamic PET-CT acquisitions. Figure SI 9A,B shows representative HPLC radiochromatograms of (**7**) prepared immediately before

injection into the animal, and non-targeted $^{64}$Cu-acetate in ammonium acetate buffer, respectively. These studies allowed us to determine the retention times for (**7**) and unbound $^{64}$Cu, which were further used to demonstrate that more than 90% of (**7**) remained intact in the urine (see Figure SI 9C) while there was no detectable activity in the feces (see Figure SI 9D).

To explore the feasibility of *in vivo* imaging and quantification of $\alpha_V\beta_3$ integrin activation in the myocardium, static *in vivo* PET-CT images were performed at 90 min after injection of (**7**) in both diabetic and non-diabetic control rats one week after myocardial infarction. To better define the right ventricular (RV) and left ventricular (LV) myocardium we administered the iodine-based X-ray contrast agent Omnipaque (GE Healthcare, USA) during CT acquisition. Representative co-registered PET-CT images are shown in Fig. 6A. PET images of (**7**) demonstrated strong focal uptake of the tracer in the infarcted area (dashed arrows), as well as in the chest wall at the site of the thoracotomy (solid arrows). The significant increase in (**7**) activity within infarcted myocardium that was observed by PET-CT imaging was confirmed by quantitative gamma well counting of myocardial sections. The retention of the radiotracer was expressed as %I.D./g tissue and graphed as circumferential Bull's eye plots for myocardial slices spanning from the apex to the base, and divided into anterior, septal, posterior and lateral sections (Fig. 6B). LAD ligation resulted in anterior-lateral infarct, which was characterized by an increased (**7**) uptake. Radioactivity within the infarcted anterior sections was approximately 4-fold higher than in non-infarcted septal regions at one week after myocardial infarction (Fig. 6C).

**Post mortem evaluation of $\alpha_V\beta_3$ expression in MI.** To investigate $\alpha_V\beta_3$ expression at the cellular level, at one week post MI, a subset of animals was euthanized, sections of the heart muscle tissue were excised, and stained with a commercially available PE-LM609 ($\alpha_V\beta_3$ marker). Subsequent fluorescence imaging showed 2.4 fold decrease in the infract tissue of DM animals in comparison to the non-DM at the one week time point with little to none change in the remote area of both groups (Fig. 7). We have also demonstrated the same trend where diabetic animals had significantly reduced (~40%, $^*P < 0.05$) myocardial uptake of (**7**) within the infarct, whereas there was no significant difference in both border and remote sections of diabetic and non-diabetic rats.

## Discussion

Dimers constitute a valuable subclass of RGD cyclopeptides, characterized by better targeting capability and higher integrin-specific uptake, when compared to their monocyclic counterparts.

In the past, a variety of linkers connecting two monomeric cyclic RGDs have been evaluated to modify radiotracer receptor binding affinity, organ uptake, biodistribution, and excretion kinetics from non-cancerous organs.

In this work, we describe the synthesis and chemical characterization of a novel dimeric cyclic-RGD probe for quantitative non-invasive imaging of $\alpha_V\beta_3$ activity followed by a multiscale biological analysis of probe's receptor binding and its pharmacokinetics. In a series of experiments we explored probe's *in vitro* binding affinity using surface plasmon resonance (SPR) with immobilized $\alpha_V\beta_3$ receptor and live endothelial cells expressing $\alpha_V\beta_3$. Finally, we evaluated the behavior of (**7**) *in vivo* and investigated its feasibility for non-invasive PET-CT imaging of $\alpha_V\beta_3$ expression following myocardial infarction in diabetic and non-diabetic animals.

We began our investigations by studying direct interactions between dimeric- and monomeric-cRGD probes and $\alpha_V\beta_3$ at the receptor level using surface plasmon resonance technique. SPR provides a powerful tool for the analysis of protein-protein and protein-ligand kinetics, including the determination of affinity, association and dissociation rates, and activation energies. SPR can be applicable even for low affinity systems which are often notoriously difficult to study using other techniques.

We demonstrated that our dimeric-cRGD construct is characterized by a very fast association to $\alpha_V\beta_3$ receptor ($k_{on} = 1.1 \times 10^7\,M^{-1}\,s^{-1}$) which is approximately 40-fold greater than that of previously characterized monomeric cRGDfK ($k_{on} = 2.7 \times 10^5\,M^{-1}\,s^{-1}$) see Table 1. In contrast, our receptor-bound dimeric-cRGD probe dissociated from the $\alpha_V\beta_3$ receptor at a much slower rate ($k_{off} = 2.1 \times 10^{-6}\,s^{-1}$) than classical adhesive proteins like fibrinogen and vibronectin ($k_{off} = 9.8 \times 10^{-4}\,s^{-1}$ and $2.1 \times 10^{-4}\,s^{-1}$, respectively)[52]. All these results suggest that both dimerization and use of certain structural elements such as PEG linkers and 1,2,3-triazole moieties, contributed to improved association to $\alpha_V\beta_3$ integrin (hence longer bound lifetime), while leaving dissociation properties essentially unchanged.

To study probe-receptor interactions at the cellular level in a biologically relevant model we used human umbilical vein endothelial cells (HUVEC), which are known to constitutively express $\alpha_V\beta_3$ integrin.

The binding affinity ($K_d$) of fluorescein (38.27 nM) and $^{64}$Cu -labeled (33.85 nM) dimeric cRGD probes were comparable to those of fibrinogen and vibronectin (27 nM and 64 nM, respectively). More importantly, the dissociation constant of our dimeric cRGD probes were approximately 20-fold smaller than most monomeric cRGD peptides, and similar to tetrameric cRGD probes reported in the literature[24]. Moreover, our dimeric-cRGD peptides have approximately only 2.5-fold lower affinity than $\alpha_V\beta_3$ integrin antibody (LM609, $K_d = 14.4$ nM), which suggests feasibility of (**7**) and (**8**) for high-sensitive targeted imaging of angiogenic activity. In addition, our tracer exhibits a nearly identical $IC_{50}$ value (5.1 nM, see Fig. 4G) as that reported for $^{18}$F-Galacto-RGD (5 nM)[53]. While we have used endothelial cells in our own assay, we note that $IC_{50}$ values can vary considerably from one cell-type to another[23]. This difference should be accounted for when comparing $IC_{50}$ across cell lines.

Certain metal ions, when bound to the $\beta_3$ subunit of $\alpha_V\beta_3$, are known to induce a conformational change that can affect the binding of cRGD ligands[54]. Manganese (II) ions, for example, activate the $\alpha_V\beta_3$ integrin, while calcium ions or strong chelators like EDTA lead to its deactivation. To study this phenomenon, we incubated HUVECs with $Mn^{2+}$ or EDTA. The addition of manganese led to a dissociation constant that was considerably lower (13.8 nM) in comparison to excess EDTA (Fig. 4A,B). These results support the notion that metal ions like $Mn^{2+}$ play an important role in mediating the interactions between $\alpha_V\beta_3$ integrin and cRGD, and illustrate the important role of environmental conditions when assessing the binding characteristics and potential of cRGD-based probes as imaging agents.

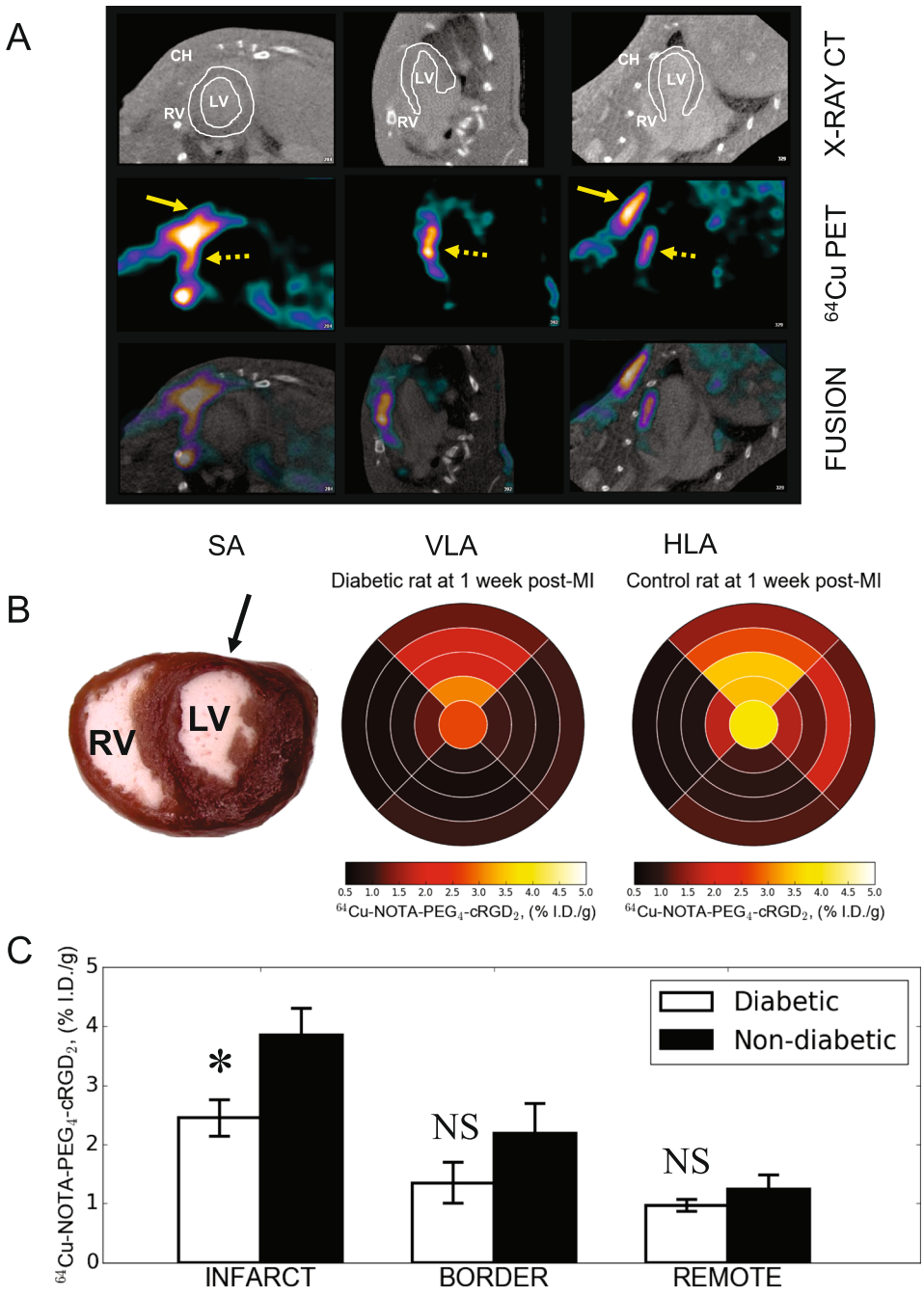


**Figure 6.** Representative *in vivo* hybrid PET-CT reconstructed short-axis (SA), vertical- (VLA) and horizontal long-axis (HLA) images acquired with iodinated contrast agent (Omnipaque) at 90 min post-injection of $^{64}$Cu-NOTA-PEG$_4$-cRGD$_2$ (**A**). The iodinated blood pool contrast agent permitted better definition of right (RV) and left ventricle (LV) within the myocardium which is contoured with solid white line. Focal uptake of $^{64}$Cu-NOTA-PEG$_4$-cRGD$_2$ was seen within anteriolateral LV regions (dashed yellow arrow) although significant uptake was seen in chest wall (CH) at the thoracotomy site (solid yellow arrows) indicating active wound healing associated $\alpha_V\beta_3$ receptor expression. Bull's eye myocardial plots of $^{64}$Cu-NOTA-PEG$_4$-cRGD$_2$ activity in diabetic and non-diabetic Lewis rats subjected to surgical ligation of LAD to induce myocardial infarction (arrow) (**B**). Hearts were immediately excised at 120 min post-injection, cleaned and filled with inert dental molding material and cut in four 2-mm thick slices from apex to base. After removing right ventricle (RV), each left ventricular (LV) slice was cut in four segments (anterior, septal, posterior, lateral), and $^{64}$Cu radioactivity was measured in each segment with gamma well counting. Data for each slice were expressed as percentage of injected dose per gram tissue (%I.D./g) and categorized as infarct, border and remote areas (**C**).

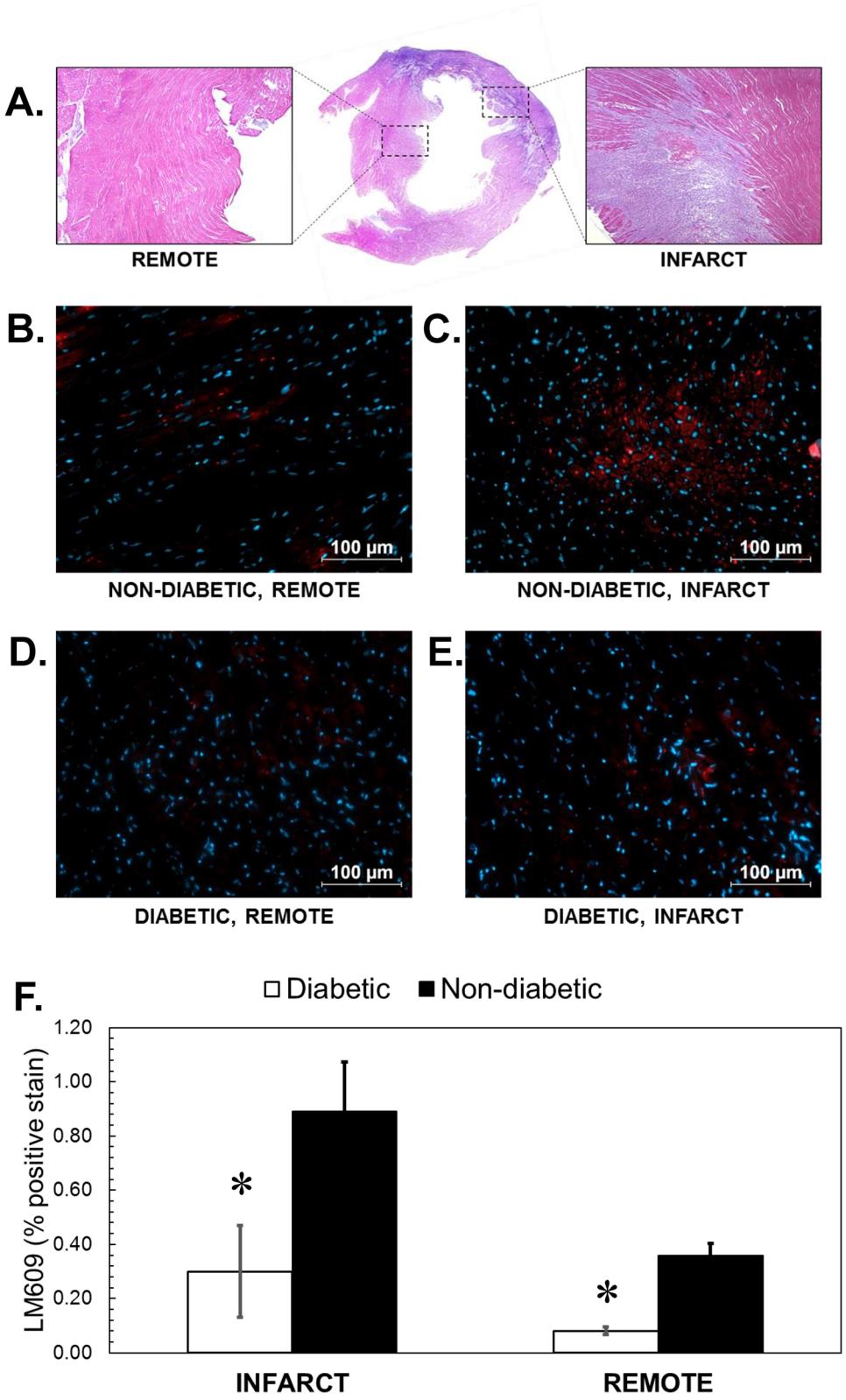


**Figure 7.** $\alpha_V\beta_3$ immunohistochemistry. (**A**) A representative H&E stain of the infarct and remote areas of the heart. (**B**–**E**) representative immunohistochemistry images with LM609 (red) and DAPI (blue). (**F**) Quantification of $\alpha_V\beta_3$ positive area in stained heart tissue. The non-DM infract tissue showed significant increase in $\alpha_V\beta_3$ expression relative to DM infract tissue.

Angiogenesis is a key factor in the process of cardiac healing after myocardial ischemia. Much work was focused at targeting angiogenesis for both diagnosis and therapy. For this reason non-invasive methods for visualizing $\alpha_V\beta_3$ after myocardial infarction using both SPECT and PET have been reported in the literature. Noteworthy examples of radio-labeled $\alpha_V\beta_3$ probes include the $^{111}$In-labeled SPECT tracer $^{111}$In–RP748, Technetium-labeled SPECT tracers like $^{99m}$Tc-RAFT-RGD, $^{99m}$Tc-IDA-D-[c(RGDfK)]$_2$, and $^{99m}$Tc-NC100692, as well as PET tracers such as $^{18}$F-Galacto-RGD, $^{68}$Ga-NODAGA-RGD, and the trimeric $^{68}$Ga-TRAP(RGD)$_3$, all of which have been studied in animal models of myocardial infarction[55–59]. PET affords higher count numbers and sensitivity than SPECT (in part because PET does not use an extrinsic collimator), and as such our probe can be used to give more sensitive images with fewer artifacts than the available SPECT tracers. Moreover, our probe utilizes $^{64}$Cu because of its favorable decay characteristics (half life 12.7 h), which allow imaging at later time points than several other commonly used PET and SPECT isotopes like $^{18}$F, $^{68}$Ga and $^{99m}$Tc (half life 110 min, 68 min, and 6 h, respectively). While the rapid pharmacokinetics of our radiotracer may speak to using a short half-life radionuclide, we chose to employ a longer half-life radioisotope which enabled our (**7**) to be more broadly applicable: the required $^{64}$Cu can be produced at a nearby cyclotron facility and then used hours to a day later without requiring the type of on-site isotope production facilities that shorter-lived isotopes do. Moreover, the NOTA chelating moiety on our probe enabled fast single step labeling (~60 min) at room temperature. Other imaging probes can require higher temperatures and much long preparation times. The preparation of $^{18}$F-Galacto-RGD, for example, requires temperatures as high as 70 °C and takes approximately 200 minutes—significantly longer than the halflife of the $^{18}$F radionuclide itself[60].

While several multimeric cRGD-based probes have been described in that past, it has been found that little sensitivity or specificity is gained by increasing the cRGD multiplicity past two cRGD units[56, 59]; as such, we have focused here on enhancing the pharmacokinetic properties of a dimeric cRDG probe. In designing the structure of our dimer we decided to employ two PEG linkers, and 1,2,3-triazole moieties. Combining both of these structural elements as pharmacokinetic modifiers was expected to improve the biodistribution and elimination of the tracer[49]. Additionally, we used NOTA when labeling with $^{64}$Cu, which has been shown to exhibit lower accumulation in the liver than other available bifunctional chelators such as DOTA[61].

The favorable effects of these structural modifications on both pharmacokinetics and organ retention were verified with dynamic PET imaging followed by biodistribution studies, which provided vital insight into the *in vivo* behavior of (**7**). Within minutes after injection, we observed a rapid blood clearance of (**7**) with paralleled retention within kidney medulla and cortex. We also observed almost complete clearance after one hour with little gastrointestinal activity (Fig. 5), which we attributed to the hydrophilicity of (**7**). We found high kidney and bladder retention, but essentially no detectable radioactivity in feces (Figure SI 9), indicating the main excretion route is through kidney filtration and urine (which has also been observed in other cRGD-based radiotracers[31, 59]).

While several previous studies of myocardial infarction employed healthy animals, here we focused specifically on imaging myocardial infarction in diabetic rats. High resolution microPET-CT imaging using (**7**) in diabetic and non-diabetic rats subjected to LAD ligation and subsequent myocardial infarction demonstrated both discrete and focal myocardial distributions (Fig. 6). Our probe was found to localize to the infarcted tissue within the anterio-lateral region of the heart, and this *in vivo* imaging pattern was obtained consistently for different rats (both diabetic and non-diabetic) at 1 week after surgical induction of myocardial infarction. Importantly, we found that the ratio of probe uptake in the infarcted region of the heart compared to a normal region was significantly higher in non-DM rats than in DM rats ($3.85 \pm 0.51$ versus $2.44 \pm 0.35$, respectively), indicating decreased $\alpha_V\beta_3$ activity and, in turn, decreased capacity for neovascularization in rats with diabetes. Similar infarcted vs. normal myocardial segments for healthy rats have been reported in prior studies ($4.7 \pm 0.8$ using $^{18}$F-Galacto-RGD, $5.2 \pm 0.8$ using $^{68}$Ga-NODAGA-RGD, and $4.1 \pm 0.7$ using $^{68}$Ga-TRAP(RGD)$_3$[55, 59]).

We found that the greatest $\alpha_V\beta_3$ activity occurred 1 week after induction of myocardial infarction in both healthy and diabetic rats, a finding in good agreement with previous studies using other RGD-based tracers in non-DM rats[58, 59]. This delayed $\alpha_V\beta_3$ uptake is a critical point to consider when designing potential stem-cell-based therapies for patients with myocardial infarction, especially those with other pathologies like diabetes that may limit their innate capacity for neovascularization. In particular, in diabetic patients, early detection and treatment could prove extremely important to myocardial infarction recovery, and to that end, rapid non-invasive imaging strategies like ours could play an important role in the clinical setting.

We demonstrated that *in vivo* targeted $\alpha_V\beta_3$ integrin imaging can be performed in combination with contrast CT imaging where the administration of X-ray contrast agent did improve the definition of the myocardial edges and the blood pool. These *in vivo* PET-CT images with contrast provided better localization of (**7**) to the site of the myocardial infarction within the anterior-lateral wall and allowed for differentiation between the myocardial wall and thoracotomy site, which was characterized by active wound healing associated $\alpha_V\beta_3$ integrin expression. Moreover, the use of the X-ray contrast agent permitted reconstruction of the $\alpha_V\beta_3$ images without the need for a reference perfusion image. Reconstruction and orientation of the PET images was extremely difficult without the reference CT images. The image properties of (**7**) are superior due to the low background activity.

This combination of both anatomical and molecular targeted imaging with dimeric-cRGD-based agents holds great promise for non-invasive quantitative assessment of different uptake patterns observed within the myocardium of diabetic and non-diabetic animals post-MI. Our results strongly suggest reduced $\alpha_V\beta_3$ integrin activation in the onset of diabetes. While the observed regional fluctuations in the radiotracer's retention remain in general agreement with previously reported observations with monomeric cRGD based SPECT and PET imaging agents or more invasive non-imaging techniques[24, 62], targeted molecular imaging with (**7**) demonstrated excellent quality images, higher or comparable specific uptake within infarcted tissue, and relatively low non-specific uptake in critical organs. All told, these imaging results clearly indicate that our dimeric-cRGD probe has a potential for quantitative mapping of spatial and temporal changes in $\alpha_V\beta_3$ activation in small animal models of myocardial injury in the onset of diabetes as well as potentially expanding these studies to larger animals and humans.

## Methods

**Synthesis and Chemical Characterization.** The synthesis and chemical characterization (NMR and HR-MS) of both (**7**) and (**8**) have been described in detail in Supplementary data (Figures S1–S8).

**Ligand-Receptor Binding Kinetics Studies.** All surface plasmon resonance (SPR) studies were performed with the BIAcore 3000 instrument (Biacore International AB, Uppsala, Sweden) at 25 °C on dextran-coated gold sensor chips (CM5, Research grade, GE Healthcare Bio-sciences AB, Uppsala) divided into four separate flow cells (three containing immobilized $\alpha_V\beta_3$ integrin receptor and one control). HBS-EP pH 7.4 (10 mmol HEPES, 3 mmol EDTA, 150 mmol NaCl, 0.002% TWEEN-20) was used as a running buffer.

Pre-concentration studies were performed to determine optimal pH conditions for receptor immobilization (Supplementary Table S1). Integrin $\alpha_V\beta_3$ receptor (R&D Systems, USA) was irreversibly immobilized to a single flow cell via amine coupling with the dextran matrix. A recombinant human CD-34 (R&D Systems, USA), a protein with no known interaction with peptides based on cRGD structure, was immobilized to a flow cell as a reference signal protein to account for non-specific interactions. Briefly, the surface was activated by injecting 35 $\mu$L of 50 mM N-hydroxysuccinimide (NHS, GE Healthcare AB) and 200 mM EDC (GE Healthcare AB) at 1:1 ratio (v/v) and a flow rate of 5 $\mu$L/min. Integrin $\alpha_V\beta_3$ receptor was dissolved at 20 $\mu$g/mL in 10 mM acetate buffer at its optimal pH and injected at 5 $\mu$L/min until the target surface immobilization level was reached (approximately 200–500 R.U. of immobilized receptor). After sufficient amount of protein was coupled, the surface was deactivated by injecting 35 $\mu$L ethanolamine.

Kinetic studies with dimeric and monomeric cRGD ligands were performed on the target flow cell containing the immobilized integrin $\alpha_V\beta_3$ receptor and the reference flow cell simultaneously. 120 $\mu$L of each ligand (10, 20, and 40 nmol in HBP-EP running buffer) was injected at 30 $\mu$L/min through both flow cells, followed by a 10 minute running buffer injection to observe ligand-receptor dissociation. After recording SPR sensograms, a series of 5 $\mu$L HCl (5 mM) and 5 $\mu$L NaOH (10 mM) at 5 $\mu$L/min was injected to remove any remaining bound ligand residues. This cycle was repeated twice for each concentration of the ligand.

The kinetic rate constants (association $k_{on}$ and dissociation $k_{off}$ constants), the goodness-of-fit parameter ($\chi^2$) and the peak magnitude of the signal response ($R_{max}$) were determined by performing global kinetic analysis on the binding curves for each ligand-receptor pair (Supplementary Data)[63–65].

**Cell Culture.** Human umbilical vein endothelial cells (HUVEC) were acquired from American Type Culture Collection (ATCC, USA) and grown to confluence in K-12 medium containing 10% heat-inactivated FBS (Invitrogen), 100 U/mL penicillin G, 100 $\mu$g/mL streptomycin, 0.25 $\mu$g/mL amphotericin B (HyClone) and were maintained in a humidified incubator at 37 °C with 5% $CO_2$.

**Cellular Binding Studies.** To investigate various cellular binding characteristics of radiolabeled (**7**) and its FITC-analogue, both gamma well counting and flow cytometry/fluorescence microscopy were used, respectively. HUVEC were incubated with (**7**) (0–100 nM) for 1 h at room temperature, filtered with 0.22 $\mu$m centrifuge filters (Corning Incorporated, USA), washed twice with PBS (pH 7.4) and radioactivity measured with gamma well counter (Wizard2, Perkin-Elmer, USA). HUVEC were also incubated in either (**8**) or FITC-Galacto-cRGD$_2$ (0–200 nM) for 1 h at room temperature. Cells were centrifuged, washed twice, and analyzed with a BD LSR II flow cytometer (BD Biosciences, USA) using gates set for FITC and corrected for auto-fluorescence. All experiments were performed in technical triplicates.

*Integrin activation and deactivation.* To study the effect of $\alpha_V\beta_3$ integrin activation/deactivation on cellular binding, HUVEC were pretreated with of $Mn^{2+}$ or EDTA (20 $\mu$M) for 10 min, washed with ice-cold PBS, and incubated with (**7**) (0–100 nM) or (**8**) (0–200 nM) for 1 h at room temperature. Cells were centrifuged, washed twice with PBS (pH 7.4), and analyzed with gamma well counter or flow cytometry using gates set for FITC and corrected for auto-fluorescence.

*Competitive binding.* HUVEC were pretreated with 50 $\mu$M of unlabeled H-PEG$_4$-cRGD$_2$ for 30 min, and then incubated with (**7**) (0–100 nM) or (**8**) (0–200 nM) for 1 h at room temperature. Cells were centrifuged, filtered with 0.22 $\mu$m centrifuge filters (Corning incorporated, USA), washed twice with PBS (pH 7.4), and analyzed with gamma well counter or flow cytometry using gates set for FITC and corrected for auto-fluorescence.

*Competitive inhibition ($IC_{50}$ determination).* HUVEC were incubated with 50 nM of (**7**) and increasing concentrations of H-PEG$_4$-cRGD$_2$ (0–1 $\mu$M) for 1 h at room temperature, filtered, and washed twice with PBS (pH 7.4), and transferred to counting tubes for gamma well counting.

*Specificity.* In order to determine the specificity to $\alpha_V\beta_3$ integrin, HUVEC were incubated with (**8**) (0.34 $\mu$M) and co-incubated with phycoerythrin (PE) conjugated anti- $\alpha_V\beta_3$ integrin antibody PE-LM609 (11.12 $\mu$g/ml) (R&D Systems, USA) for 1 h at room temperature. Cells were centrifuged at 5000 rpm for 10 min and washed twice with ice-cold PBS (pH 7.4). Gates were set for PE, FITC, and corrected for auto-fluorescence and potential overlap between the PE and FITC channels.

*Dual-fluorescence staining.* HUVEC were grown to confluence on coverslips and fixed with 4% paraformaldehyde for dual-fluorescence staining with (**8**) (1 $\mu$M) and anti- $\alpha_V\beta_3$ PE-LM609 antibody (1:100, R&D Systems, USA). The coverslips were incubated with each stain separately for 1 h at room temperature, with washing buffer (PBS, pH 7.4) rinses before and after each incubation for a duration of 5 min. Coverslips were mounted to slides with DAPI Fluoromount (Southern Biotech, USA), imaged with a confocal fluorescence inverted microscope

(Zeiss LSM 700 Confocal, Germany) equipped with 63x oil objective, preprocessed with commercial software package (ZEN 2012, Zeiss, USA), and colocalization analyzed with Fiji software[66].

**In Vivo Evaluation.** *Animal preparation.* All *in vivo* imaging experiments were approved by the Institutional Animal Care and Use Committee of the University of Illinois at Urbana-Champaign, in accordance to the principles outlined by the American Physiological Society on research animal use.

*Blood clearance, metabolism and biodistribution.* To assess blood clearance and organ uptake dynamic *in vivo* PET-CT imaging was performed followed by image processing and analysis. Lewis rats (n = 6, Harlan Inc.) were anesthetized with 2% isoflurane, the neck area was shaved and a jugular vein cut-down procedure was performed to insert a PE-50 polyurethane catheter for radiotracer injection. Animals were then placed in supine position on the polyacrylic imaging bed of a small animal dedicated PET-CT scanner (Inveon, Siemens Healthcare, USA). At the time of PET acquisition, animals were injected with ~22.2 MBq of (**7**) via the jugular vein catheter over 30 s followed by bolus infusion of 0.2 mL sterile saline. Animals underwent 60 min dynamic PET imaging (15% energy window centered at 511 keV) followed by anatomical X-ray CT imaging (80 keV, 500 $\mu$A, 100 $\mu$m spatial resolution).

Following dynamic PET-CT imaging, both urine and feces samples were collected to assess radiotracer's metabolism and excretion route. The urine samples were collected at 90 min post injection by manual void, mixed at 1:1 ratio (v/v) with 50% $CH_3$ CN and centrifuged at 5000 rpm. The supernatant was collected, analyzed by HPLC (C18 column, flow 1 mL/min, $CH_3$ OH/$H_2$ O, 5/95, v/v), and chromatograms compared to reference samples of (**7**) and $^{64}$Cu-acetate. Feces samples were collected at 90 min post injection, suspended in 50% $CH_3$ CN, homogenized and centrifuged at 5000 rpm. The supernatant was filtered and analyzed by RP-HPLC.

For biodistribution studies, all animals were euthanized at 90 min post-injection and selected organ samples were collected for gamma well counting analysis. All collected sections were weighed and the tissue radioactivity was measured with Wizard$^2$ gamma well counter (Perkin-Elmer, USA). Measured $^{64}$Cu activity was corrected for background, decay time, and tissue weight.

*In vivo imaging of myocardial angiogenesis.* To evaluate the feasibility of (**7**) imaging in rodent model of myocardial ischemia, male diabetic and non-diabetic Lewis rats (n = 5 in each group) were subjected to surgical permanent ligation of left anterior descending (LAD) artery to induce anteriolateral myocardial infarction (MI) resulting in angiogenic response[62]. Type-1 diabetes was induced by bolus injection of 50 mg/kg streptozotocin (STZ), which resulted in hyperglycemia (>200 mg/dl glucose) and glucosuria at 6 weeks post STZ injection. To induce MI, animals were anesthetized with 1–3% isoflurane, and the respiration was controlled using an animal ventilator (Kent Scientific, USA) for a thoracotomy incision. Myocardial infarction was induced by ligating the proximal LAD coronary artery with 8–0 silk suture. One week after the surgery, all animals were anesthetized with 1–3% isoflurane, neck area shaved, and the left jugular vein was isolated for placement of a PE-50 polyurethane catheter to facilitate injection of the radiotracer. All animals were injected with ~29.6 MBq of (**7**). Imaging was performed using hybrid small animal microPET-CT scanner (Inveon, Siemens Healthcare, USA). Animals were placed on animal bed and ~60 min after radiotracer injection, a 15 min microPET imaging was performed. This was followed by a high-resolution anatomical microCT imaging (360 projections, 80 keV/500 $\mu$A energy) during continuous (0.8 mL/min) intravenous infusion of an X-ray CT contrast agent (Omnipaque, GE Healthcare, USA) using programmable syringe pump (Kent Scientific, USA).

*Image analysis and tissue processing.* The microPET and microCT images were reconstructed using OSEM/3D iterative algorithm (Siemens Healthcare, USA) and cone-beam technique (Cobra Exim), respectively. Both microPET and microCT images were fused, reoriented and visualized as short (SA), vertical- (VLA) and horizontal-long (HLA) axis slices using Inveon Research Workplace (Siemens Healthcare, USA). Immediately after last imaging session, all animals were euthanized with intravenous injection of KCl (1 mol/L), hearts excised and washed in ice-cold buffered saline. Both right and left ventricles were filled with dental molding material to facilitate uniform cutting into 2 mm slices. All slices were then divided into four sections; anterior, lateral, posterior and septal. Collected sections were weighed and tissue radioactivity was measured with Wizard2 gamma well counter (Perkin-Elmer, USA). Measured $^{64}$Cu activity was corrected for background, decay time, and tissue weight, and expressed as percent injected dose (% I.D./g).

*Histology and immunochemistry.* A subset of the animals were euthanized at 1 week post surgery and their heart tissue were excised, embedded in TissueTec (Sakura, USA) and snap frozen in −150 °C methylbutane. Frozen sections (5 nm) were placed on microscope slides, fixed with pre-cooled acetone, and stored at −80 °C before staining. To assess heart muscle vascularity, heart samples were stained with an $\alpha_V\beta_3$ marker PE-LM609 Antibody (Abcam, USA). All staining procedures were performed according to the product-specific protocols (four for each slide). The stains were quantified for extent (percentage area) of positive staining in randomly chosen high-powered (200x) fields using algorithms validated by our group previously[57].

## Conclusions

During the last decade, much effort has been expended on the chemical modification of RGD peptides to increase affinity for $\alpha_V\beta_3$ integrin. Recent studies suggested that cyclic RGD dimers have high affinity due to bivalency and have relatively low non-specific uptake in other critical organs. These properties can be further optimized by modification of the distance between the two RGD motifs using PEG linkers. It was also shown that introduction of 1,2,3-triazole moieties has a positive impact on the pharmacokinetic profile of receptor-binding ligands. All of this has been taken into consideration during the development of our dimeric cRGD probe. This study described

the synthesis, chemical characterization, and multi-scale biological evaluation of both radiolabeled and fluorescent dimeric RGD peptide ligands for molecular imaging of $\alpha_V\beta_3$ integrin activation at the receptor, single cell, organ and whole-body level. Here we demonstrated that the targeted PET-CT imaging of regional activation of $\alpha_V\beta_3$ integrin within ischemic tissue holds the potential to directly quantify the extent and localization of ongoing angiogenic process *in vivo* and to assess this process on cellular level *in vitro* using optical imaging with a fluorescent analogue of the targeted imaging agent. The enhanced focal retention, favorable blood clearance kinetics and biodistribution, and excellent quality of images obtained with (**7**) suggest the potential for future clinical translation. This and other molecular imaging-based approaches should lead to better understanding of pathophysiology and development of novel paradigms for patient management.

## References


1. Folkman, J. Angiogenesis in cancer, vascular, rheumatoid and other disease. *Nat Med* **1**, 27–30, doi:10.1038/nm0195-27 (1995).
2. Dobrucki, L. W., de Muinck, E. D., Lindner, J. R. & Sinusas, A. J. Approaches to multimodality imaging of angiogenesis. *J Nucl Med* **51**(Suppl 1), 66S–79S, doi:10.2967/jnumed.109.074963 (2010).
3. Otrock, Z. K., Mahfouz, R. A., Makarem, J. A. & Shamseddine, A. I. Understanding the biology of angiogenesis: review of the most important molecular mechanisms. *Blood Cells Mol Dis* **39**, 212–20, doi:10.1016/j.bcmd.2007.04.001 (2007).
4. Yamada, M. Molecular interactions in cell adhesion complexes. *Curr Opin Cell Biol* **9**, 76–85, doi:10.1016/S0955-0674(97)80155-X (1997).
5. Shattil, S. J., Kim, C. & Ginsberg, M. H. The final steps of integrin activation: the end game. *Nat Rev Mol Cell Biol* **11**, 288–300, doi:10.1038/nrm2871 (2010).
6. Xiong, J.-P. *et al*. Crystal structure of the extracellular segment of integrin αvβ3. *Science* **294**, 339–345, doi:10.1126/science.1064535 (2001).
7. Niu, G. & Chen, X. Why integrin as a primary target for imaging and therapy. *Theranostics* **1**, 30–47, doi:10.7150/thno/v01p0030 (2011).
8. Goswami, S. Importance of integrin receptors in the field of pharmaceutical & medical science. *Adv Biol Chem* **3**, 224–252, doi:10.4236/abc.2013.32028 (2013).
9. Cai, W., Niu, G. & Chen, X. Imaging of integrins as biomarkers for tumor angiogenesis. *Curr Pharm Des* **14**, 2943–73, doi:10.2174/138161208786404308 (2008).
10. Zhang, Y., Yang, Y. & Cai, W. Multimodality imaging of integrin $\alpha_V\beta_3$ expression. *Theranostics* **1**, 135–148, doi:10.7150/thno/v01p0135 (2011).
11. Iagaru, A. & Gambhir, S. S. Imaging tumor angiogenesis: the road to clinical utility. *AJR Am J Roentgenol* **201**, W183–91, doi:10.2214/AJR.12.8568 (2013).
12. Liu, Y., Yang, Y. & Zhang, C. A concise review of magnetic resonance molecular imaging of tumor angiogenesis by targeting integrin alphavbeta3 with magnetic probes. *Int J Nanomedicine* **8**, 1083–1093, doi:10.2147/IJN.S39880 (2013).
13. Haubner, R. & Decristoforo, C. Radiolabelled rgd peptides and peptidomimetics for tumour targeting. *Front Biosci (Landmark Ed)* **14**, 872–86, doi:10.2741/3283 (2009).
14. Schottelius, M., Laufer, B., Kessler, H. & Wester, H. J. Ligands for mapping alphavbeta3-integrin expression *in vivo*. *Acc Chem Res* **42**, 969–80, doi:10.1021/ar800243b (2009).
15. Liu, S. Radiolabeled cyclic rgd peptides as integrin alpha(v)beta(3)-targeted radiotracers: maximizing binding affinity via bivalency. *Bioconjug Chem* **20**, 2199–213, doi:10.1021/bc900167c (2009).
16. Zhou, Y., Chakraborty, S. & Liu, S. Radiolabeled cyclic rgd peptides as radiotracers for imaging tumors and thrombosis by spect. *Theranostics* **1**, 58–82, doi:10.7150/thno/v01p0058 (2011).
17. Danhier, F., Le Breton, A. & Preat, V. Rgd-based strategies to target alpha(v) beta(3) integrin in cancer therapy and diagnosis. *Mol Pharm* **9**, 2961–73, doi:10.1021/mp3002733 (2012).
18. Tateishi, U., Oka, T. & Inoue, T. Radiolabeled rgd peptides as integrin alpha(v)beta3-targeted pet tracers. *Curr Med Chem* **19**, 3301–9, doi:10.2174/092986712801215937 (2012).
19. Cai, H. & Conti, P. S. Rgd-based pet tracers for imaging receptor integrin alphav beta3 expression. *J Labelled Comp Radiopharm* **56**, 264–79, doi:10.1002/jlcr.2999 (2013).
20. Haubner, R., Maschauer, S. & Prante, O. Pet radiopharmaceuticals for imaging integrin expression: tracers in clinical studies and recent developments. *Biomed Res Int* **2014**, 871609, doi:10.1155/2014/871609 (2014).
21. Gaertner, F. C., Kessler, H., Wester, H. J., Schwaiger, M. & Beer, A. J. Radiolabelled rgd peptides for imaging and therapy. *Eur J Nucl Med Mol Imaging* **39**(Suppl 1), S126–38, doi:10.1007/s00259-011-2028-1 (2012).
22. Beer, A. J., Kessler, H., Wester, H. J. & Schwaiger, M. PET Imaging of Integrin $\alpha_V\beta_3$ Expression. *Theranostics* **1**, 48–57, doi:10.1007/s10555-008-9158-3 (2011).
23. Liu, S. Radiolabeled cyclic rgd peptide bioconjugates as radiotracers targeting multiple integrins. *Bioconjug Chem* **26**, 1413–38, doi:10.1021/acs.bioconjchem.5b00327 (2015).
24. Gao, H. *et al*. Pet imaging of angiogenesis after myocardial infarction/reperfusion using a one-step labeled integrin-targeted tracer 18f-alf-nota-prgd2. *Eur J Nucl Med Mol Imaging* **39**, 683–92, doi:10.1007/s00259-011-2052-1 (2012).
25. Eo, J. S. *et al*. Angiogenesis imaging in myocardial infarction using 68ga-nota-rgd pet: characterization and application to therapeutic efficacy monitoring in rats. *Coron Artery Dis* **24**, 303–11, doi:10.1097/MCA.0b013e3283608c32 (2013).
26. Kiugel, M. *et al*. Dimeric [(68)ga]dota-rgd peptide targeting alphavbeta 3 integrin reveals extracellular matrix alterations after myocardial infarction. *Mol Imaging Biol* **16**, 793–801, doi:10.1007/s11307-014-0752-1 (2014).
27. Reyes, E. A novel pet tracer for targeted imaging of atherosclerosis. *J Nucl Cardiol* **22**, 1191–4, doi:10.1007/s12350-015-0088-5 (2015).
28. Mammen, M., Choi, S.-K. & Whitesides, G. M. Polyvalent interactions in biological systems: Implications for design and use of multivalent ligands and inhibitors. *Angewandte Chemie* **37**, 2754–2794, doi:10.1002/(sici)1521-3773(19981102)37:20<2754::aid-anie2754>3.0.co;2-3 (1998).
29. Chen, X. *et al*. Micropet imaging of breast cancer alphav-integrin expression with 64cu-labeled dimeric rgd peptides. *Mol Imaging Biol* **6**, 350–9, doi:10.1016/j.mibio.2004.06.004 (2004).
30. Chen, X. *et al*. Micro-pet imaging of alphav-beta3-integrin expression with 18f-labeled dimeric rgd peptide. *Mol Imaging* **3**, 96–104, doi:10.1162/1535350041464892 (2004).
31. Li, Z. B. *et al*. (64)cu-labeled tetrameric and octameric rgd peptides for small-animal pet of tumor alpha(v)beta(3) integrin expression. *J Nucl Med* **48**, 1162–71, doi:10.2967/jnumed.107.039859 (2007).
32. Li, Z. B., Chen, K. & Chen, X. (68)ga-labeled multimeric rgd peptides for micropet imaging of integrin alpha(v)beta (3) expression. *Eur J Nucl Med Mol Imaging* **35**, 1100–8, doi:10.1007/s00259-007-0692-y (2008).
33. Liu, S. *et al*. Evaluation of a (99 m)tc-labeled cyclic rgd tetramer for noninvasive imaging integrin alpha(v)beta3-positive breast cancer. *Bioconjug Chem* **18**, 438–46, doi:10.1021/bc0603081 (2007).
34. Wang, L. *et al*. Improving tumor-targeting capability and pharmacokinetics of (99 m)tc-labeled cyclic rgd dimers with peg(4) linkers. *Mol Pharm* **6**, 231–45, doi:10.1021/mp800150r (2009).

35. Shi, J. *et al*. Improving tumor uptake and pharmacokinetics of (64)cu-labeled cyclic rgd peptide dimers with gly(3) and peg(4) linkers. *Bioconjug Chem* **20**, 750–9, doi:10.1021/bc800455p (2009).
36. Kubas, H. *et al*. Multivalent cyclic rgd ligands: influence of linker lengths on receptor binding. *Nucl Med Biol* **37**, 885–91, doi:10.1016/j.nucmedbio.2010.06.005 (2010).
37. Shi, J. *et al*. Evaluation of in-labeled cyclic rgd peptides: Effects of peptide and linker multiplicity on their tumor uptake, excretion kinetics and metabolic stability. *Theranostics* **1**, 322–40, doi:10.7150/thno/v01p0322 (2011).
38. Ji, S. *et al*. (99 m)tc-galacto-rgd2: a novel 99mtc-labeled cyclic rgd peptide dimer useful for tumor imaging. *Mol Pharm* **10**, 3304–14, doi:10.1021/mp400085d (2013).
39. Goodman, S. L. & Picard, M. Integrins as therapeutic targets. *Trends Pharmacol Sci* **33**, 405–12, doi:10.1016/j.tips.2012.04.002 (2012).
40. Ma, Q. *et al*. Differential diagnosis of solitary pulmonary nodules using (9)(9)mtc-3p(4)-rgd(2) scintigraphy. *Eur J Nucl Med Mol Imaging* **38**, 2145–52, doi:10.1007/s00259-011-1901-2 (2011).
41. $^{99m}$tc-3prgd$_2$ for integrin receptor imaging of lung cancer: a multicenter study. *J Nucl Med* **53**, 716–722, doi:10.2967/jnumed.111.098988 (2012).
42. Miao, W. *et al*. Comparison of 99mtc-3prgd2 integrin receptor imaging with 99mtc-mdp bone scan in diagnosis of bone metastasis in patients with lung cancer: a multicenter study. *PLoS One* **9**, e111221, doi:10.1371/journal.pone.0111221 (2014).
43. Liu, L. *et al*. (99)mtc-3prgd2 scintimammography in palpable and nonpalpable breast lesions. *Mol Imaging* **13**, doi:10.2310/7290.2014.00010 (2014).
44. Mittra, E. S. *et al*. Pilot pharmacokinetic and dosimetric studies of (18)f-fpprgd2: a pet radiopharmaceutical agent for imaging alpha (v) beta (3) integrin levels. *Radiology* **260**, 182–91, doi:10.1148/radiol.11101139 (2011).
45. Iagaru, A. *et al*. (18)f-fpprgd2 pet/ct: pilot phase evaluation of breast cancer patients. *Radiology* **273**, 549–59, doi:10.1148/radiol.14140028 (2014).
46. Minamimoto, R. *et al*. Biodistribution of the (1) (8) f-fpprgd (2) pet radiopharmaceutical in cancer patients: an atlas of suv measurements. *Eur J Nucl Med Mol Imaging* **42**, 1850–8, doi:10.1007/s00259-015-3096-4 (2015).
47. Iagaru, A. *et al*. Glioblastoma multiforme recurrence: An exploratory study of (18)f fpprgd2 pet/ct. *Radiology* **277**, 497–506, doi:10.1148/radiol.2015141550 (2015).
48. Withofs, N. *et al*. 18f-fprgd2 pet/ct imaging of integrin alphavbeta3 in renal carcinomas: correlation with histopathology. *J Nucl Med* **56**, 361–4, doi:10.2967/jnumed.114.149021 (2015).
49. Walsh, J. C. & Kolb, H. C. Applications of click chemistry in radiopharmaceutical development. *Chimia (Aarau)* **64**, 29–33, doi:10.2533/chimia.2010.29 (2010).
50. Chen, K. *et al*. Synthesis and evaluation of 64cu-labeled monomeric and dimeric ngr peptides for micropet imaging of cd13 receptor expression. *Mol Pharm* **10**, 417–27, doi:10.1021/mp3005676 (2013).
51. Bentz, J. *et al*. Variability in p-glycoprotein inhibitory potency (ic(5)(0)) using various *in vitro* experimental systems: implications for universal digoxin drug-drug interaction risk assessment decision criteria. *Drug Metab Dispos* **41**, 1347–66, doi:10.1124/dmd.112.050500 (2013).
52. Urbinati, C. *et al*. alpha(v)beta3-integrin-dependent activation of focal adhesion kinase mediates nf-kappab activation and motogenic activity by hiv-1 tat in endothelial cells. *J Cell Sci* **118**, 3949–58, doi:10.1242/jcs.02518 (2005).
53. Haubner, R. *et al*. Noninvasive imaging of alpha(v)beta3 integrin expression using 18f-labeled rgd-containing glycopeptide and positron emission tomography. *Cancer Res* **61**, 1781–5, doi:Published March 2001 (2001).
54. Takagi, J., Petre, B. M., Walz, T. & Springer, T. A. Global conformational rearrangements in integrin extracellular domains in outside-in and inside-out signaling. *Cell* **110**, 599–11, doi:S0092867402009352 [pii] (2002).
55. Higuchi, T. *et al*. Assessment of alphavbeta3 integrin expression after myocardial infarction by positron emission tomography. *Cardiovasc Res* **78**, 395–403, doi:10.1093/cvr/cvn033 (2008).
56. Meoli, D. F. *et al*. Noninvasive imaging of myocardial angiogenesis following experimental myocardial infarction. *J Clin Invest* **113**, 1684–91, doi:10.1172/JCI20352 (2004).
57. Hua, J. *et al*. Noninvasive imaging of angiogenesis with a 99mtc-labeled peptide targeted at alphavbeta3 integrin after murine hindlimb ischemia. *Circulation* **111**, 3255–60, doi:10.1161/CIRCULATIONAHA.104.485029 (2005).
58. Dimastromatteo, J. *et al*. *In vivo* molecular imaging of myocardial angiogenesis using the alpha(v)beta3 integrin- targeted tracer 99mtc-raft-rgd. *J Nucl Cardiol* **17**, 435–43, doi:10.1007/s12350-010-9191-9 (2010).
59. Laitinen, I. *et al*. Comparison of cyclic rgd peptides for alphavbeta3 integrin detection in a rat model of myocardial infarction. *EJNMMI Res* **3**, 38, doi:10.1186/2191-219X-3-38 (2013).
60. Haubner, R. *et al*. [18f]galacto-rgd: synthesis, radiolabeling, metabolic stability, and radiation dose estimates. *Bioconjug Chem* **15**, 61–9, doi:10.1021/bc034170n (2004).
61. Garrison, J. C. *et al*. *In vivo* evaluation and small-animal pet/ct of a prostate cancer mouse model using 64cu bombesin analogs: side-by-side comparison of the cb-te2a and dota chelation systems. *J Nucl Med* **48**, 1327–37, doi:10.2967/jnumed.107.039487 (2007).
62. Dobrucki, L. W. *et al*. Analysis of angiogenesis induced by local igf-1 expression after myocardial infarction using microspect-ct imaging. *J Mol Cell Cardiol* **48**, 1071–9, doi:10.1016/j.yjmcc.2009.10.008 (2010).
63. Biacore, A. *BIAevaluation Software Handbook 4* (1997).
64. Karlsson, R. Affinity analysis of non-steady-state data obtained under mass transport limited conditions using biacore technology. *J Mol Recognit* **12**, 285–92, doi:10.1002/(SICI)1099-1352(199909/10)12:5<285::AID-JMR469>3.0.CO;2-Y (1999).
65. Murphy, M., Jason-Moller, L. & Bruno, J. Using biacore to measure the binding kinetics of an antibody-antigen interaction. *Curr Protoc Protein Sci* Chapter 19, Unit 19 14, doi:10.1002/0471142301.ps1914s45 (2006).
66. Schindelin, J. *et al*. Fiji: an open-source platform for biological-image analysis. *Nat Methods* **9**, 676–82, doi:10.1038/nmeth.2019 (2012).


## Acknowledgements

Studies were funded by AHA Scientist Development Grant (10SDG4180043, LWD), Arnold Beckman Foundation (LWD, ID), Ministry of Science and Higher Education Poland ("Mobility Plus" Program, AP), Foundation for Polish Science (TEAM/2011-7/5, LK), and Peptides International Inc.

## Author Contributions

L.W.D., J.H., L.K., P.I., A.C., P.S. designed the experiments. J.H., A.P., A.C., M.S., S.M., P.S., L.L., I.D. performed the experiments. L.W.D., J.H., A.C. wrote the manuscript. J.C., A.C., P.C., P.S. helped with the data analyses. L.W.D., P.I., J.C., A.C., M.B. read and reviewed the manuscript.

## Additional Information

**Supplementary information** accompanies this paper at doi:10.1038/s41598-017-03224-8

**Competing Interests:** The authors declare that they have no competing interests.